ADVANCED INTELLIGENT SYSTEMS
Open Access
www.advintellsyst.com

All-Electric Nonassociative Learning in Nickel Oxide

Sandip Mondal, Zhen Zhang, A. N. M. Nafiul Islam, Robert Andrawis, Sampath Gamage, Neda Alsadat Aghamiri, Qi Wang, Hua Zhou, Fanny Rodolakis, Richard Tran, Jasleen Kaur, Chi Chen, Shyue Ping Ong, Abhronil Sengupta, Yohannes Abate, Kaushik Roy, and Shriram Ramanathan*

Habituation and sensitization represent nonassociative learning mechanisms in both non-neural and neural organisms. They are essential for a range of functions from survival to adaptation in dynamic environments. Design of hardware for neuroinspired computing strives to emulate such features driven by electric bias and can also be incorporated into neural network algorithms. Herein, cellular-like learning in oxygen-deficient NiO_x devices is demonstrated. Both habituation learning and sensitization response can be achieved in a single device by simply controlling the magnitude of the electric field. Spontaneous memory relaxations and dynamic redistribution of oxygen vacancies under electric bias enable such learning behavior of NiO_x under sequential training. These characteristics in simple device arrays are implemented to learn alphabets as well as demonstrate simulated algorithmic use cases in digit recognition. Transition metal oxides with carefully prepared defect concentrations can be highly sensitive to electronic structure perturbations under moderate electrical stimulus and serve as building blocks for next-generation neuroinspired computing hardware.

1. Introduction

Cells comprise fundamental, structural, functional, and biological elements of living organisms and are capable of learning new information through training.[1–3] Cells can acquire knowledge from previous incidents and react accordingly to a new situation, a critical survival instinct which is a universal feature of all organisms.[4–6] Cellular-like learning can occur genomically (**Figure 1**a), where a gene memorizes[7,8] and transmits the learnt information to the future generation upon cell divisions referred to as epigenetic learning.[5,9,10] There are different types of epigenetic cellular-like learning observed wherein habituation and sensitization are two elementary nonassociative learning forms.[11,12] Epigenetic habituation learning can be defined as a decrease in the magnitude of reaction to an iterative training cycle that enables the organism to ignore repetitive stimuli.[13] The epigenetic habituation occurs when the input to a gene carries to output with a negative genomic regulator which is marked as inhibitory (Figure 1b). As a result, the output reduces due to the memorization of inhibitory negative epigenetic marking upon recurring stimuli. In the case of sensitization (Figure 1c), the behavioral output of a gene is the opposite of habituation that indicates an increase in response with respect to the recurring stimulus. When the inputs are given to the gene, the output

S. Mondal,[+] Z. Zhang, Q. Wang, S. Ramanathan
School of Materials Engineering
Purdue University
West Lafayette, IN 47907, USA
E-mail: sandip@ee.iitb.ac.in

A. N. M. N. Islam, A. Sengupta
School of Electrical Engineering and Computer Science
The Pennsylvania State University
University Park, PA 16802, USA

The ORCID identification number(s) for the author(s) of this article can be found under https://doi.org/10.1002/aisy.202200069.

[+]Present address: Department of Electrical Engineering, Indian Institute of Technology (IIT) Bombay, Powai, Mumbai 400076, India

DOI: 10.1002/aisy.202200069

R. Andrawis, K. Roy
School of Electrical and Computer Engineering
Purdue University
West Lafayette, IN 47907, USA

S. Gamage, N. A. Aghamiri, Y. Abate
Department of Physics and Astronomy
University of Georgia
Athens, GA 30602, USA

H. Zhou, F. Rodolakis
X-ray Science Division
Advanced Photon Source
Argonne National Laboratory
Lemont, IL 60439, USA

R. Tran, J. Kaur, C. Chen, S. P. Ong
Department of NanoEngineering
University of California San Diego
9500 Gilman Dr, Mail Code 0448, La Jolla, CA 92093-0448, USA

J. Kaur
Department of Materials Science & Engineering
University of California San Diego
9500 Gilman Dr, Mail Code 0448, La Jolla, CA 92093-0448, USA

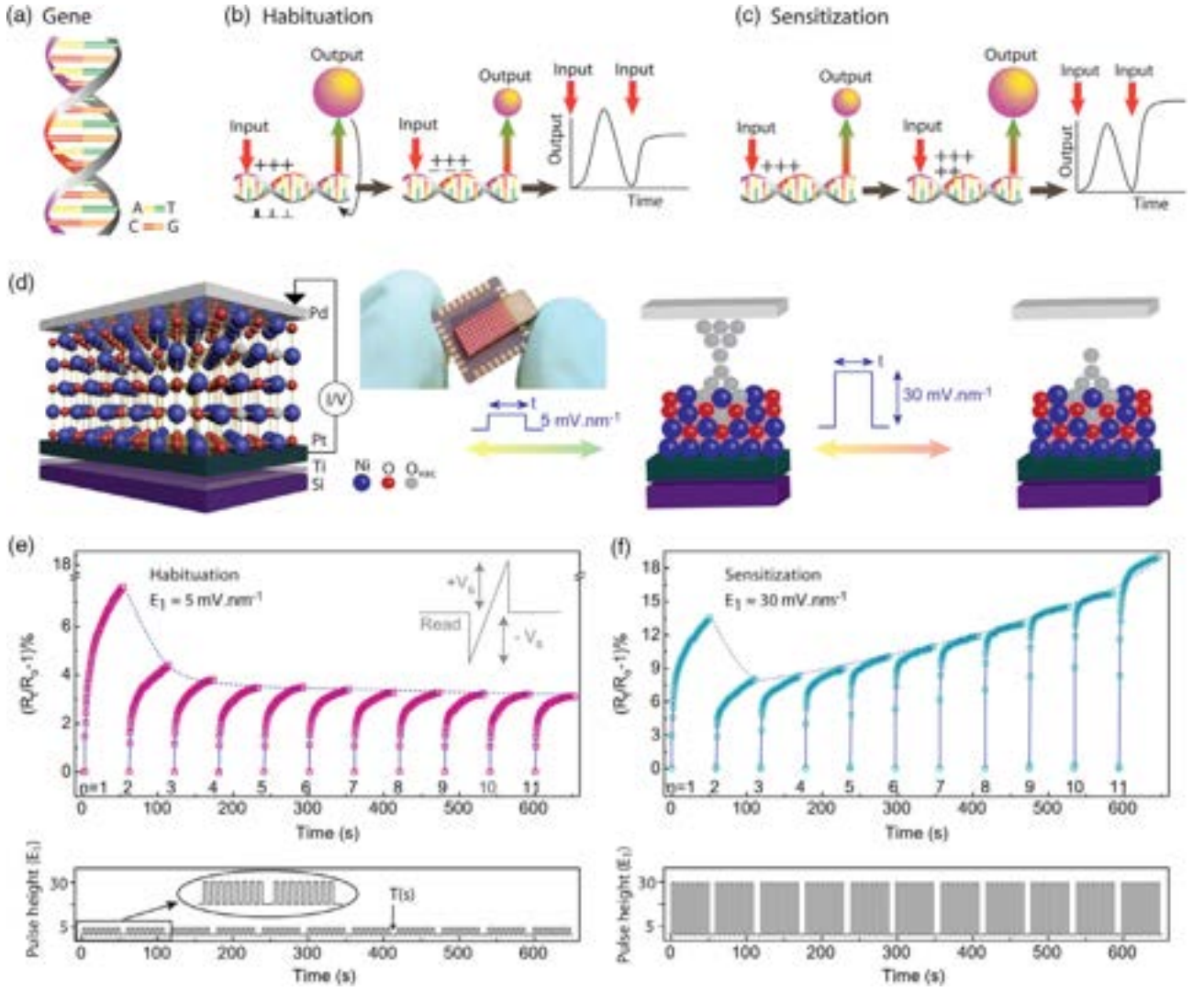

Figure 1. Nonassociative learning in NiO_x. a) Schematic of a gene (DNA). b) Habituation indicates a reduction in the response after repetitive exposure to stimuli. c) Sensitization implies an increase in response with respect to the iterative stimulus. The positive/negative signs represent marked genes with respect to inputs (training). d) Schematic of NiO_x device architecture. The input training pulses were applied between the top (Pd) and bottom (Pt) electrode which causes movement of oxygen vacancies depending on the amplitude of the pulses. (inset) Optical image of an array of NiO_x test chip. e–f) Relative percentage change in resistance with respect to the training times when each training cycle was performed for 52 s with an interval of $T = 8$ s. The pulse width was kept constant to 500 ms with the amplitude of input pulses of $E_1 = 5$ mV nm^{-1} for habituation (e) and 30 mV nm^{-1} for sensitization (f). (inset) Triangular pulses used for measuring the change in resistance state. (bottom panels) Square-shaped training pulse series applied to the device for the habituation and sensitization measurement.

increases with repetitive input correspondingly. Emulation of epigenetic behavior in synthetic matter is still in early stages due to complex requirements of electrical stimulus-sensitive history-dependent metastable states in the materials which can respond, remember, and forget input signals.[14] In electronic devices, migration of charged defects such as oxygen vacancies can help realize distinct resistance states corresponding to the learning process. By manipulating their response to electrical stimulus, different forms of learning may be realized. This provides an analogy to the processes mediated by biological matter in cells.

At the outset, it is important to note that nonassociative learning is distinct from commonly reported synaptic potentiation and depression in artificial synapses (Figure S1, Supporting Information). Potentiation and depression involves either positive or negative training electric pulses applied without regard to the specific time interval.[15,16] On the other hand, habituation and sensitization learning plasticity (Figure S1b,c, Supporting Information) are studied under multiple electrical training events including consideration of the relaxation time processes. During the interval period in habituation and sensitization training, no external stimulus is applied and the system spontaneously begins to relax. Furthermore, nonassociative learning expects increase or decrease of response with respect to the training number for identical stimulus, whereas potentiation and

depression do not necessarily rely on such variation in response. This necessitates the need for complex energy landscapes with characteristic stimuli-sensitive timescales of relaxing to the ground state. Emulating nonassociative learning has drawn substantial interest in brain-inspired computing and information processing as it is a fundamental form of learning.[17] Habituation and sensitization learning are present in various organisms and is essential to enhance their survival.[18] Nonassociative learning has been realized in traditional very-large-scale integration technology using a large number of transistors (≈20) as well as other electronic components. These powerful circuits are capable of image processing as well as image recognition with improved efficiency and highly accurate feature extraction.[19–21] There is interest in emulating such features in nonsilicon devices in the emerging fields of neuromorphic computing.[22]

Mimicry of nonassociative learning using the single-resistive two-terminal oxide-based solid-state device is promising to reduce circuit-level complexity.[14,15] To date, environmental habituation has been demonstrated by switching between different gases (e.g., H_2, O_3, and Ar) at high temperatures in nickel-based oxides.[23,24] However, an electric field-driven solid-state device which can emulate nonassociative learning is still lacking. Indeed, a large body of literature exists on potentiation and depression[15,16] and forgetting behavior[25–29] using different types of oxide memristors including NiO but their response under sequential electrical training and relaxation sessions is unknown.[16]

Here, we emulate nonassociative learning behavior using electric bias in solid-state devices from the oxygen-deficient binary nickel oxide (henceforth referred to as NiO_x wherein $x < 1$) at room temperature. A typical schematic of the NiO_x-based solid-state device architecture is shown in Figure 1d and S2, Supporting Information. Both habituation and sensitization behavior are demonstrated in the same solid-state device simply by controlling different amplitudes of training pulses that are independent of repetition intervals of electrical stimulation. We relate the temporal reduction of relative resistance modulation to habituation which occurs due to dispersion of oxygen vacancies near the electrode by the low amplitude of electric field ($E_1 = 5\ \mathrm{mV\,nm^{-1}}$). A higher electric field ($E_1 = 30\ \mathrm{mV\,nm^{-1}}$) reduces excess oxygen vacancies near the top electrode that enhances the response of the resistance state corresponding to sensitization. We then present a nonassociative learning model related to habituation and sensitization based on comparator theory.[30]

2. All Electric Nonassociative Learning in NiO_x

The training of NiO_x has been performed by applying a series of input electrical pulses. During training, the pulse amplitude (E_1) was retained constant to $5\ \mathrm{mV\,nm^{-1}}$ and width of 0.5 s for a repetition interval (T) of 8 s (Figure 1e and S3, Supporting Information). The NiO_x device shows a higher response to the training cycle and demonstrates a change in relative resistance of 7.6% after the first training cycle. The relative resistance change reduces to 4.4% and 3.8% after the second and third training cycles, respectively. The response of the NiO_x device gradually decreases with the repetition of training cycles, indicating habituation to electric pulses. On the other hand, the response of NiO_x continuously increases when the training pulses were applied with higher amplitude (E_1) of $30\ \mathrm{mV\,nm^{-1}}$ by keeping exactly identical pulse width and repetition interval as used for the habituation experiment (Figure 1f and S3, Supporting Information). The early response of the device was found to be 13.6% (first training cycle) and then decreased 8% (second training cycle), indicating initial habituation; however, the response starts to increase after the second training cycle consistent with response noted in biology during sensitization measurements.[31] The response of the devices becomes equivalent to the initial response (≈13%) after eight training cycles, a significant increase in the response to 19% when the 11th cycle of training pulses was applied to the devices. Such increase in response with respect to the electrical training is a measure of sensitization behavior similar to what is noted in cellular organisms, shown in Figure 1c.

3. Statistics of Nonassociative Learning

The response of the NiO_x device has been measured after the complete withdrawal of electrical stimulus for prolonged time (**Figure 2**a,b). The NiO_x device demonstrates complete recovery to its original resistive state and reproducibility of learning characteristics as the successive electrical training results in habituation and sensitization. The habituation experiment was performed by applying training pulses with amplitude and width of $5\ \mathrm{mV\,nm^{-1}}$ and 0.5 s, respectively. The NiO_x device continues to demonstrate habituation behavior with respect to the training cycle even after 24 h of withdrawal of training pulses in ambient (Figure 2a). A similar measurement was performed for the sensitization experiments by applying a higher amplitude of training pulses of $30\ \mathrm{mV\,nm^{-1}}$ (Figure 2b). Here, the number of pulses applied for the training is similar to habituation cycles. The habituation and sensitization response of the devices has been reproduced with the same magnitude even after long rest time in air. Thus, nonassociative learning occurs in the solid-state system even if the stimulus is withdrawn for a prolonged time analogous to what is observed in neuroscience studies.[30]

In order to investigate the dependency of nonassociative learning in the presence of electrical stimuli, a set of experiments has been performed by varying the training interval (T). The effect of training interval (T) on habituation and sensitization experiments has been investigated by varying T from 6 to 52 s for a constant training time (Figure S4, Supporting Information). The device shows habituation and sensitization behavior irrespective of the repetition interval (Figure 2c,d). Further, the dependency of learning behavior on the amplitude of training pulses has been studied by varying amplitudes of training pulses where pulse width and training intervals were set to 0.5 s and $T = 8$ s, respectively (Figure S5, Supporting Information). The device demonstrates habituation behavior for the pulse amplitude (E_1) varied from 5 to $15\ \mathrm{mV\,nm^{-1}}$, whereas the sensitization is observed at $25\ \mathrm{mV\,nm^{-1}}$ and above (Figure 2e). A crossover response is observed from the device for a pulse amplitude of $20\ \mathrm{mV\,nm^{-1}}$, implying the learning behavior manifested by the strength of electric pulses, where the lower amplitude of

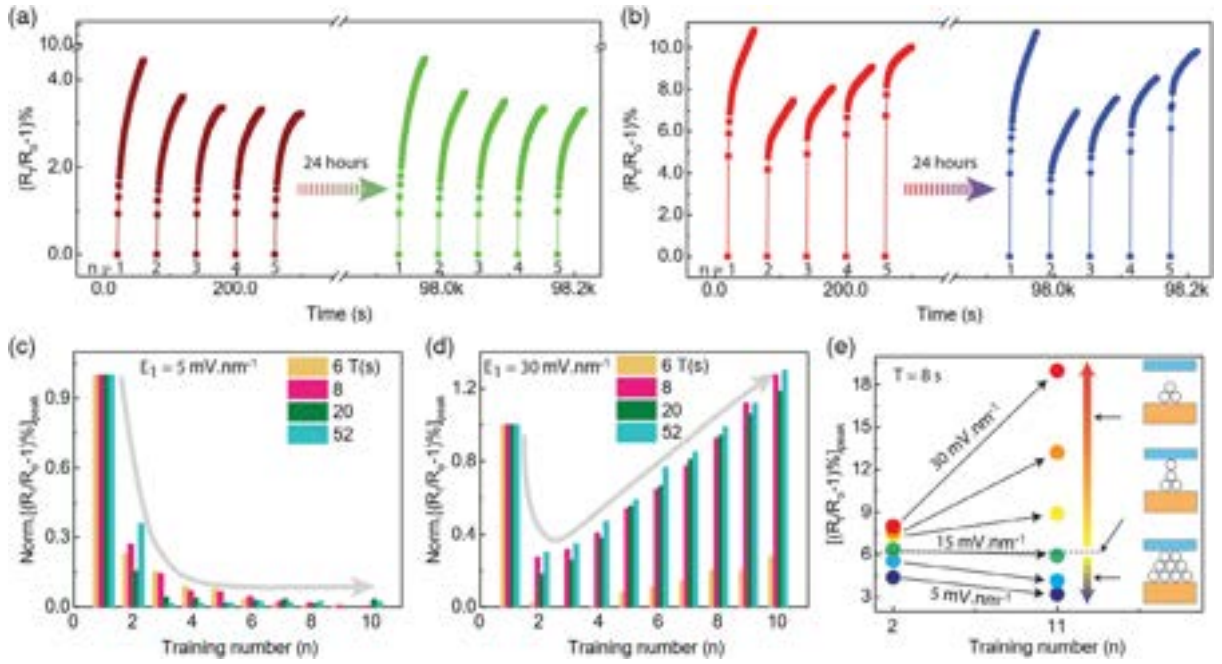

Figure 2. Training interval and bias amplitude-dependent habituation and sensitization. a,b) Habituation and sensitization measurement was executed by following the resting time of 24 h and applying training electric field of 5 and 30 mV nm^{-1}, respectively. The NiO_x device returns to the original resistive response after long rest period in normal laboratory environment. c) Training interval (T) dependence of the NiO_x device with a constant pulse amplitude $E_1 = 5$ mV nm^{-1}. The arrow indicates habituation in an electric field even after training interval T of 52 s, which is equal to the training time. d) Sensitization of NiO_x with $E_1 = 30$ mV nm^{-1} for different training intervals. The increased response is independent of the training interval. e) Amplitude of training pulse (E_1) dependence of NiO_x with a constant training interval $T = 8$ s. The critical electric field between habituation and sensitization is about 20 mV nm^{-1}. (Inset) Movement of oxygen vacancies at different training pulses.

the pulses is responsible to create habituation and the higher amplitude of pulses is capable of generating sensitization behavior, indicating a controllable learning capability of NiO_x with respect to the selected electric field.

4. Electrothermal Physics Model for Habituation and Sensitization

The nonassociative learning of NiO_x devices has been investigated qualitatively using a simple electrothermal physics model based on the concentration of oxygen vacancies near the electrode interface (Figure S6, Supporting Information). The model represents the oxygen vacancy motion near the electrode which is primarily responsible for nonassociative learning. The as-prepared NiO_x contains a large number of oxygen vacancies (deposition conditions specifically chosen to create an oxygen-deficient oxide) that forms conducting pathways.[32] Iterative training cycle with lower amplitude leads to decrease in oxygen concentration and accumulation of more oxygen vacancies near the top electrode, hence lowering the resistive response, representing habituation. On the other hand, the higher amplitude of electrical pulses is capable of dispersing the oxygen vacancies near ≈10 nm of the top electrode, indicating disruptions of conducting filaments, leading to a higher response to the relative change in resistance, leading to sensitization behavior.

5. Cellular-like Learning Model

According to the stimulus model comparator theory,[29] when a noxious stimulus is presented repeatedly, the organism generates a model for the incoming stimulus. With the further appearance of a noxious stimulus, the strength of the experienced stimulus will be compared and the response generated accordingly. The experienced stimulus must be remembered for a short period of time for comparison purposes, indicating a short-term memory-like model as proposed in **Figure 3**a. This model proposes, if there is no stimulus within a short period of time, the previous memory will erase completely, and the organism will respond as if it is a new stimulus. However, the memorization level increases with respect to the strength of the stimulus, indicating higher chance of survival even in an unpleasant environment. Here, two types of stimulus have been used for retraining, where a weak stimulus causes habituation and strong stimulus leads to sensitization.

To benchmark against the comparator model, the adaptive forgetting mechanism (i.e., retention behavior) of NiO_x has been investigated under different stimulus strengths (Figure 3b). A decay relaxation time has been extracted for different pulse amplitudes (inset of Figure 3b). It has been observed that the relaxation time enhances for increased pulse amplitude. Moreover, the forgetting behavior has been studied by applying repetitive electric pulses (50 training pulses) on the devices (Figure 3c), demonstrating 10X longer time memory retention

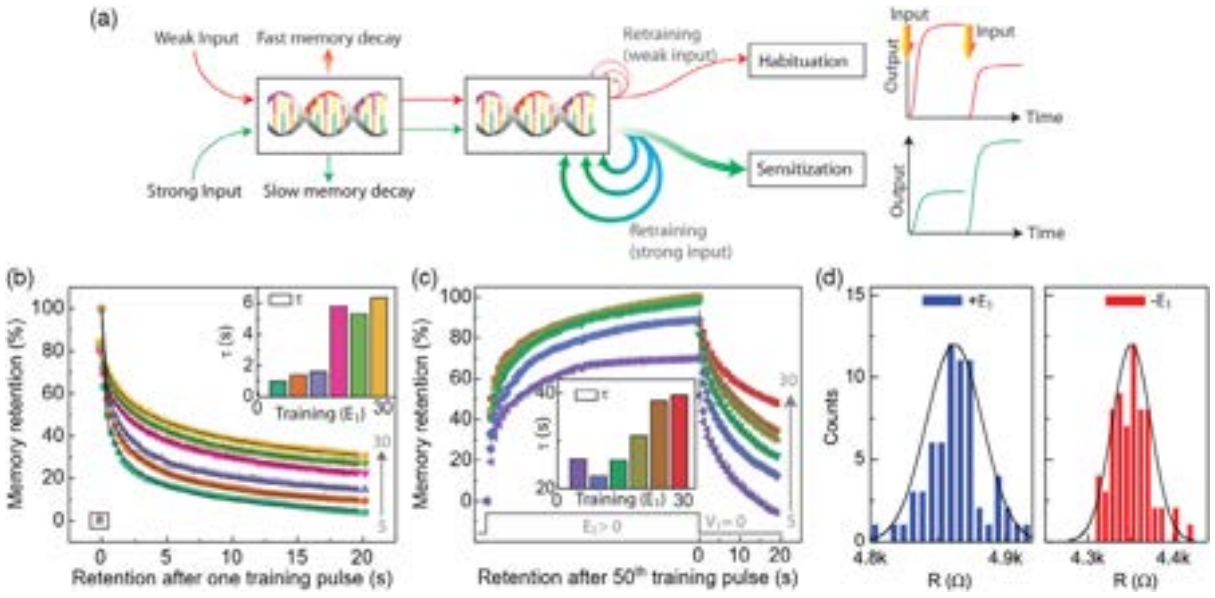

Figure 3. Habituation and sensitization model based on "stimulus model comparator theory.[30]" a) A proposed model on habituation and sensitization based on retraining using weak and strong stimulus (inputs), respectively. b,c) The resistance decay behavior of NiO_x has been compared with the decay time constant (τ), extracted from the decay curve by fitting the exponential relation, $\Delta R(t)/\Delta R_o = \exp[1-(t/\tau)^{\beta}]$, where, $\Delta R(t) = R(t) - R_{pristine}$ and $\Delta R_o = R_o - R_{pristine}$ in which R (t) is the resistance at any specific time t and R_o is the resistance measured immediately after applying b) single and c) 50 training pulses and index β ranging from 0 to 1. (insets) τ representing relaxation time constant with respect to the amplitude of training pulses. d) A statistical distribution of memory window was collected from 65 devices measured immediately after applying the pulses of $\pm 30\ mV\ nm^{-1}$ for 500 ms.

compared with a single training pulse (inset of Figure 3c). This result is quite consistent with the forgetting behavior proposed by Ebbinghaus,[33] suggesting requirements of retraining.

To examine the device-to-device reproducibility of the resistive switching window, we fabricated 65 devices on a chip and measured the switching properties follow by space-charge-limited conduction mechanism analysis (Figure 3d and S7, Supporting Information). The histogram of the switching window demonstrates a higher resistive state concentrated at 4.86 kΩ, where 90% of the device lies within the switching window of 4.86 kΩ ± 45 Ω, for the switching pulse of $+30\ mV\ nm^{-1}$ with a pulse width 0.5 s. The devices also exhibit a lower resistive state, statistically concentrated at 4.35 kΩ with a variation of ±58Ω, while a switching pulse of $-30\ mV\ nm^{-1}$ was applied to the devices with similar pulse width. The device-to-device variation of the switching state (ΔΩ/Ωmean) is found to be less than 2%, indicating scalability of the devices. In addition, every device shows a wide memory window with respect to the pulse width and demonstrates potentiation and depression (Figure S8, Supporting Information).

6. Elementary Mechanisms Leading to Learning in NiO_x

Various types of resistive memory behaviors have been observed in NiO_x ranging from bistable memory switching, monostable threshold switching, to nonassociative learning reported in this work (Table S1, Supporting Information, compiles an exhaustive list of switching studies on NiO). Essentially, the stoichiometry of Ni:O in the compound determined by oxygen partial pressure during synthesis greatly influences the resulting behavior under electric fields (Table S2, Supporting Information), for example, threshold switching behavior was observed in oxygen-rich and near-stoichiometric samples.[34] On the contrary, in this work, the NiO_x samples showing nonassociative learning behavior were grown in an oxygen-starved environment (Figure S9, Supporting Information). In order to study the role of oxygen vacancies in realizing the learning behavior, the as-prepared NiO_x samples were annealed at different temperatures up to 450 °C in air. After annealing at different temperatures up to 450 °C, the resistivity of the films increases from 10^6 to $10^8\ \Omega\ cm$ (**Figure 4**a), indicating the annihilation of oxygen vacancies during postannealing. The reduction in oxygen vacancy concentration upon air annealing was further investigated using the combination of synchrotron spectroscopy and first-principle modeling as discussed next. NiO_x devices fabricated from as-grown samples demonstrate stable switching under an electric field (E_1) of $\pm 30\ mV\ nm^{-1}/0.5$ s, as shown in Figure 4b and S10, Supporting Information. Moreover, the as-prepared device shows a continuous update of current when multiple current–voltage sweeps were performed continuously (Figure S11, Supporting Information). After annealing at 450 °C for 1 h in air, the NiO_x device does not display any switching behavior even under higher electric field (Figure 4b).[35,36] Analysis of the carrier density from midinfrared scattering-type scanning near-field optical microscopy (s-SNOM) is presented in Figure 4c, which indicates a greater free carrier density in as-grown samples (see Experimental Section for details). The resistance switching characteristics are found only in

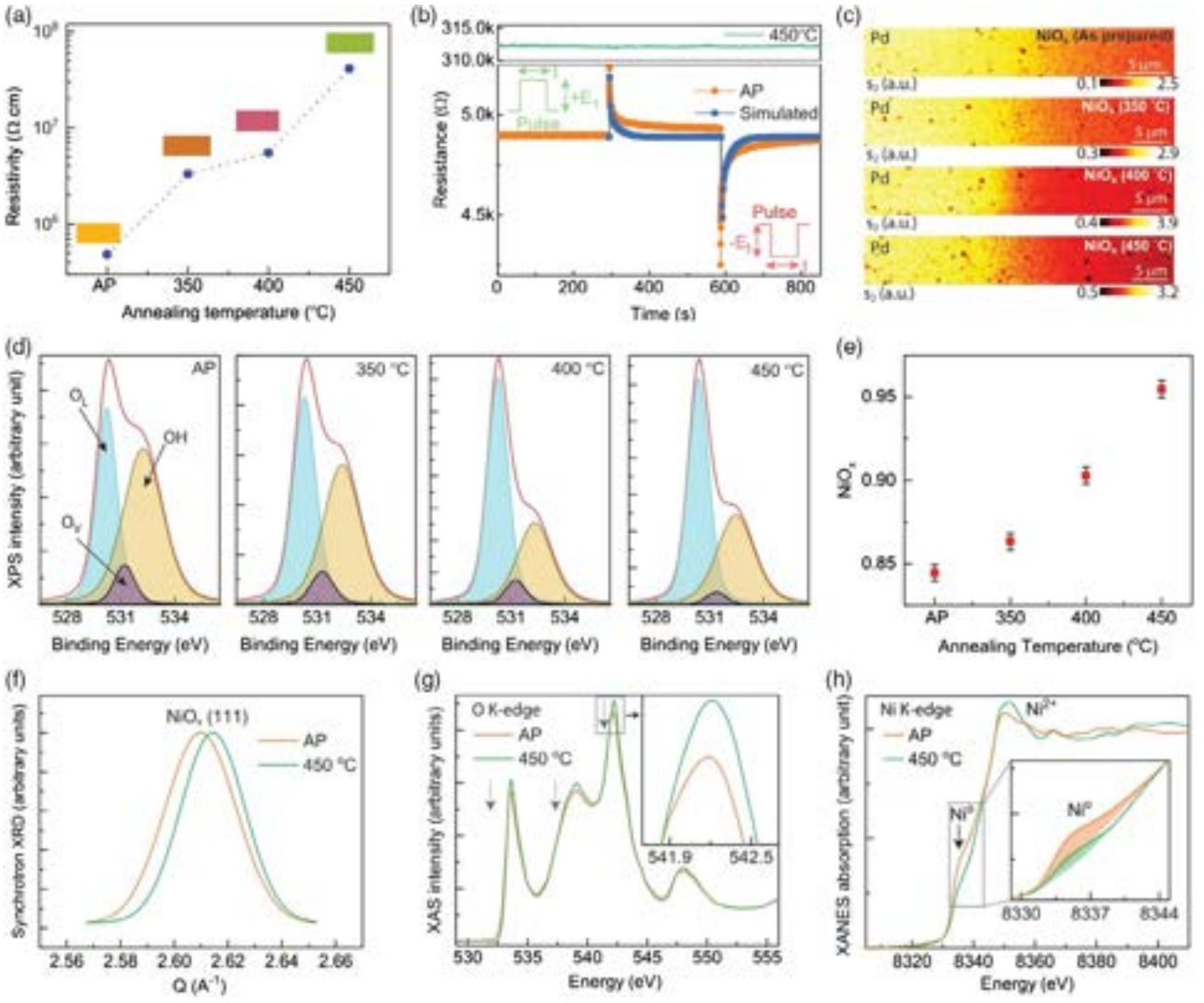

Figure 4. Mechanisms enabling cellular-like learning in oxygen-deficient NiO_x. a) Electrical resistivity with visual color change in NiO_x films after annealing at different temperature (Figure S2, Supporting Information). b) (bottom) Optimal resistive switching state in the as-prepared (AP) NiO_x is essential for cellular-like learning. The resistance increases from 4.7 kΩ (pristine) to 5.2 kΩ for application pulse width of $+30$ mV nm^{-1}/0.5 s and decreases to 4 kΩ owing to the application of -30 mV nm^{-1}/0.5 s. The simulated curve follows the trends of switching characteristics. (Top) After the heat treatment at 450 °C/1 h, the device does not display any switching behavior due to the annihilation of oxygen vacancies. c) s-SNOM second-harmonic amplitude images taken at laser wavelength of $\lambda = 10.5$ μm of NiO_x samples prepared in 2% oxygen environment and annealed at different temperatures (as prepared, 350 °C, 400 °C, and 450 °C). d) Oxygen peaks in core level measured by XPS for as-prepared to 450 °C-annealed NiO_x films, respectively. The oxygen peaks fit by three distinct components corresponding to lattice oxygen (O_L) are cyan, oxygen vacancies (O_V) violet, and hydroxide (O_{OH}) yellow. e) Stoichiometry of NiO_x, where x denotes the ratio of oxygen to nickel. f) Synchrotron X-ray diffraction of NiO_x (111) peaks after annealing. Lattice constant expansion of ≈0.19% is observed for AP NiO_x over 450 °C NiO_x film. g) Ex situ XANES-measured spectrum for AP NiO_x and after annealing. The weight of the O K-edge peaks reduces (arrow direction) for AP NiO_x, indicating a decrease of unoccupied state in O 2p orbital with higher oxygen vacancies. (inset) Zoomed peak intensity variation. h) Normalized Ni K-edge XANES spectra of AP NiO_x and 450 °C NiO_x with pre-edge features in zoomed view (inset).

oxygen-deficient films. The defect states in NiO_x film can be further characterized by X-ray photoelectron spectroscopy (XPS) by measurement of O 1s peak and Ni 2p peaks (Figure S12, Supporting Information). As Figure 4d shows, the O1s XPS peak is split into oxygen vacancies (O_V) and lattice oxygen (O_L) and hydroxide (OH).[37,38] A noticeable reduction in O_V peak for the air-annealed NiO_x device indicates an approach toward stoichiometric composition ($NiO_{0.97}$ after annealing at 450 °C)[39] (Figure 4e). On the other hand, the as-prepared NiO_x film contains higher concentration of oxygen vacancies ($NiO_{0.85}$) (Figure S13, Supporting Information). Similar trends are observed by Raman spectroscopy (Figure S14, Supporting Information).

The films were further characterized using synchrotron X-ray diffraction, as shown in Figure 4f. A shift of NiO_x (111) diffraction peak to higher Q ($=2\pi/d$) value after annealing at 450 °C

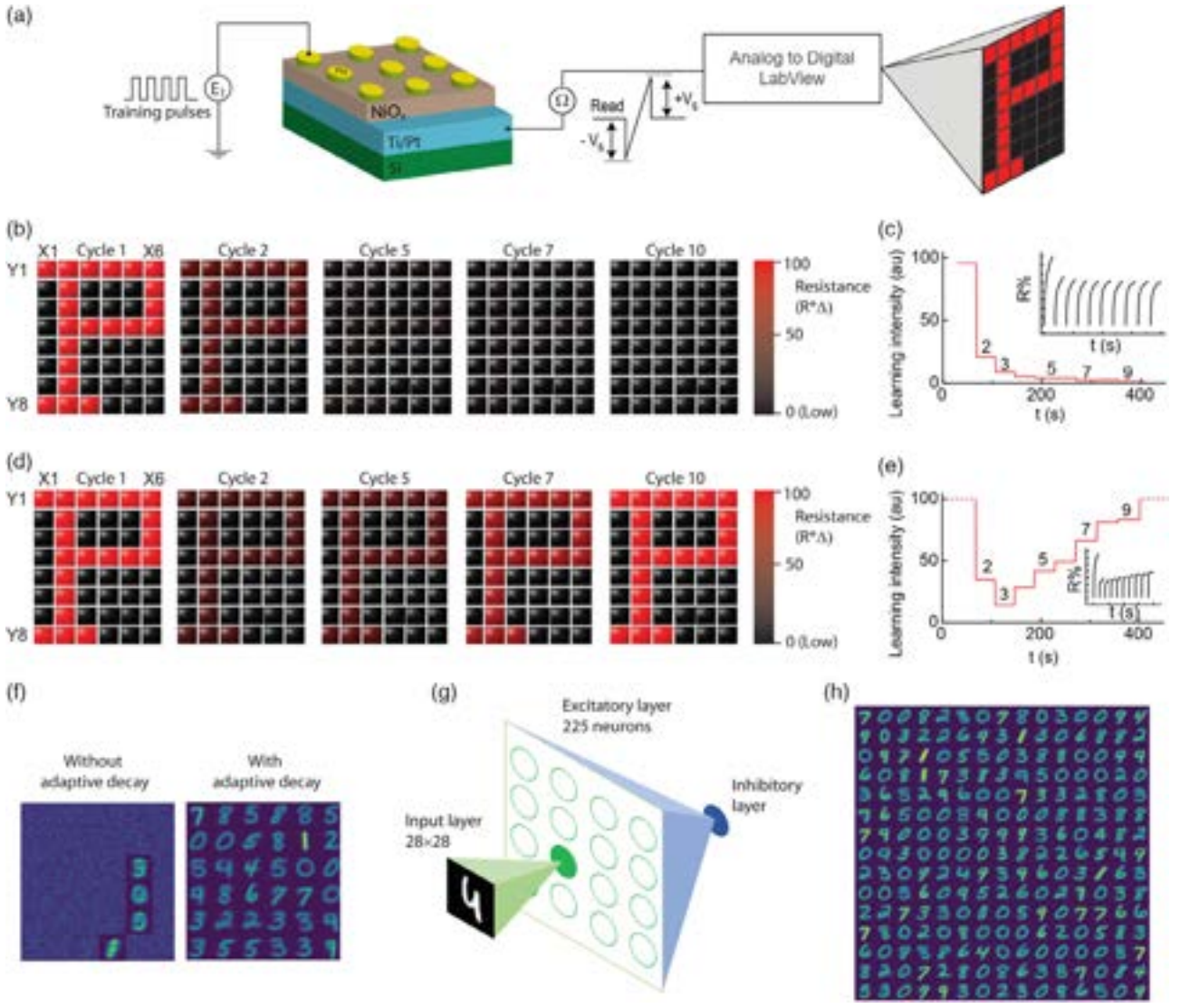

Figure 5. Proof-of-concept learning with NiO_x device arrays and implementation of homeostatic regulation. a) The light intensity of letter "P" has been controlled by 6×8 of NiO_x devices corresponding to change in resistance with respect to the training cycle. b) The training has been performed by applying 50 training pulses amplitude $E_1 = 5$ mV nm^{-1} and width 500 ms (Video S1, Supporting Information). The delay between training pulses was kept constant to 8 s. c) A systematic change in light intensity is recorded with respect to time demonstrating the occurrence of habituation. The intensity was scaled with respect to the first training cycle. d) Sensitization measurement has been performed by applying a similar number of training pulses of amplitude $E_1 = 30$ mV nm^{-1} and width 500 ms. The intensity of "P" increases due to the continuous training process after the initial decrease of intensity (Video S2, Supporting Information). Here, the intensity is scaled into tenth training pulse. e) Systematic change in intensity at different training cycles has been recorded. (insets) Change in resistance for *X*–*Y* after every training cycle for habituation and sensitization respectively. f) Effect of neuronal adaptive decay realizing homeostasis on a toy network. Without adaptively changing the decay rate (no homeostasis), only a few neurons fire and dominate. In contrast, adaptive decay functionality in the neuronal devices provides an alternate pathway to enable homeostasis in the network, thereby allowing all neurons to competitively learn. g) The network architecture consisting of an input layer of size equal to the dimensionality of the MNIST training images, an excitatory layer of 225 LIF neurons with adaptive decay, and an inhibitory neuron layer for implementing lateral inhibition. h) The final weight patterns after training over the 60 000 training images. The network achieves an accuracy of 84.8% over the test set of 10 000 images.

corresponds to a decrease in the lattice constant (d) by 0.19%. The as-prepared (AP) NiO_x sample has larger concentration of oxygen vacancies, which results in lattice expansion. Additional X-ray absorption spectroscopy (XAS) measurements have been performed to investigate oxygen vacancies in AP-NiO_x (Figure 4g). The lower weight of O-K-edge for AP-NiO_x demonstrates less unoccupied states of O 2*p* orbitals accompanied with the oxygen deficiency and is consistent with first-principles calculations (Figure S15, Supporting Information). After annealing, the as-prepared NiO_x becomes more stochiometric as the spectrum weight of the 450 °C-annealed NiO_x shifts to lower energy in Ni L-edge (Figure S16, Supporting Information). The X-ray absorption near-edge structure (XANES) spectra of Ni-K-edge demonstrate a feature of Ni^0 and Ni^{2+}, which indicates the

appearance of oxygen vacancies in the system[40] (Figure 4h). After annealing at 450 °C, the Ni^0 feature becomes suppressed corresponding to the annihilation of oxygen vacancies during annealing (inset of Figure 4h).

7. Proof-of-Concept Application of Nonassociative Learning in a Device Array

To illustrate nonassociative learning behavior, habituation and sensitization experiments have been carried out on a 6×8 array grid, as shown in **Figure 5**. The NiO_x device array attempts to learn an alphabet "P" in the presence of an electric field, where the intensity of light-emitting diode (LED) bulb is a measure of learning (Figure 5a). The habituation measurement has been performed by applying 50 training pulses with an amplitude of 5 mV nm^{-1} for 0.5 s in each training cycle. Every training cycle was performed at an interval of 8 s (Figure 5b and Movie S1, Supporting Information). After the first training cycle, the array of NiO_x devices learnt to program "P" with the highest intensity of LEDs. Further decrease in learning intensity to 20% is observed after the second training cycle. The change in intensity with respect to the training cycle is summarized in Figure 5c. A dramatic reduction in intensity close to zero is found after the tenth training cycle, indicating habituation. In contrast, a higher amplitude of electric field ($E_1 = 30$ mV nm^{-1}) causes enhancement in intensity even after using the constant value of other parameters that have been used for habituation measurement (Figure 5d). The enhancement in the intensity of LED array with respect to the training cycle of NiO_x is analogous to the level of sensitization noted in biological organisms (Figure 5e and Movie S2, Supporting Information).

8. Proof-of-Concept Application of Nonassociative Learning in Spiking Neural Network (SNN)

In neuroinspired systems, AI models have looked at learning from various levels of abstraction—focusing either on modeling the synaptic phenomenon of short-term plasticity[24,41] or on modulating the excitability of neuronal dynamics.[42] Here, we focus on the neuron activity modulation scenario and showcase that the cellular-like learning in NiO_x can be used to implement homeostatic regulation in neurons,[43] essential for stability while learning. Homeostasis ensures a neuron, that has fired before, finds it harder to fire in the future (requires a greater input than previously). Similar to habituation, this ensures that a target level of activity is maintained in the network, with no single neuron dominating the firing pattern (Figure 5f). Implementation of temporal spiking neuron dynamics like the leaky–integrate–fire (LIF) model[44] augmented with homeostasis effects involves significant hardware overhead in complementary metal–oxide–semiconductor (CMOS) implementations. For instance, analog CMOS designs with transistors in subthreshold saturation regime involve complex feedback circuitry to implement homeostasis and consist of more than 20 transistors.[45,46] In contrast, NiO_x devices can be used to mimic the leaky–integrate dynamics of the membrane potential with homeostasis at a one-to-one level through its intrinsic physics by leveraging its decay time modulation property as a function of the operating electric field (Figure S17, Supporting Information). Using the device dynamics, we demonstrate this capability in a system-level application with a large-scale network simulation for learning handwritten digits from the MNIST dataset.[47] Our network (Figure 5g) with 225 neurons attained an accuracy of 84.8% on the MNIST test set—on par with networks of similar size.[48–50] The network with the adaptive decay scheme was able to implement homeostasis—inducing competition with no single neuron dominating (Figure 5h).

9. Conclusion

Oxygen-deficient NiO_x shows resistance switching under electric bias and spontaneous relaxation of memory. This combination of material properties enables demonstration of all-electric nonassociative learning: simple control of electric field shows switching between habituation and sensitization modes in a single device. Mott materials sensitive to electrical excitations can serve as building blocks to explore features of evolutionary biology for implementation in machine intelligence.

10. Experimental Section

Synthesis of NiO_x Films: The NiO_x film was grown from a pure Ni target, using magnetron sputtering with a power of 100 W, where the applied voltage and current were controlled to 350 V and 300 mA (direct current), respectively. The NiO_x film was grown at a pressure of 5 mTorr with flow of 1 sccm O_2 (2%) and 49 sccm (98%) Ar gas mixture. The film was grown at a temperature of 300 °C with a rate of $\approx$3 nm min^{-1}. To achieve a uniform film, the substrate rotated with a speed of 20 rpm during deposition. To compare with devices made from the pristine NiO_x film, we further annealed the NiO_x films at elevated temperatures (i.e. 350 °C, 400 °C, and 450 °C, respectively) for 1 hr in air.

Device Fabrication: A schematic of a typical two-terminal metal–oxide–metal (MOM) cellular-like device architecture is depicted in Figure 1d. NiO_x was deposited by a completely inorganic, carbon-free, magnetron sputtering method on Ti/Pt (10/70 nm)-coated silicon substrate (p-Si, 100). At first, the silicon substrates were cleaned with a triple-cleaning method using toluene, acetone, and isopropanol by sonicating for 5 min each and dry blown with N_2 gas. The silicon wafer was heated to 200 °C to remove the moisture from the surface before depositing the Ti/Pt metal. The bottom metal contact (Ti/Pt) was grown by e-beam evaporation. Then the wafer was transferred into the deposition chamber to grow 96 nm NiO_x film. After the growth of the NiO_x film, the substrate was transferred to another sputtering chamber with a circular shadow mask to deposit the top metal electrode. A 200 nm palladium (Pd) top electrode was deposited by sputtering at 10^{-3} mbar pressure. All cellular-like devices were stored in ambient environments.

In Situ Electrical Measurements: The electrical characterization of the solid-state NiO_x devices was performed by constantly measuring the current–voltage (I–V) curves by sweeping the gate voltage from −10 to 10 mV with a step of 5 mV using the Keithley 2635 A source meter. The measurements were performed in a closed shield probe station to avoid electrical noise from the surroundings. The habituation and sensitization training in the array of devices were performed by applying square pulses to the devices connecting them in parallel to the Keithley 2635 A source meter. The resistance measurement was accomplished using LabVIEW programming and connecting to the 6×8 LED bulbs.

X-ray Absorption Spectroscopy: Absorption spectroscopy at the O K-edge and Ni L-edge of NiO_x thin films was performed at beamline 29-ID-D at the Advanced Photon Source, Argonne National Laboratory. Data were collected simultaneously in total electron yield (TEY) and total fluorescence

yield (TFY) at room temperature in a pressure better than 5×10^{-8} Torr. TFY signal was collected using a microchannel plate located at 54° with 7° angular acceptance. The incidence angle was set to 30°. Circular-polarized X-ray with an overall energy resolution better than 100 meV was used. Using the drain current from a gold mesh upstream of the sample, both absorption signals were normalized by the incident X-ray intensity. The XANES spectra at the absorption K-edge of Ni of the NiO_x thin films were taken under ambient temperature and pressure at the beamline 33-ID-D of Advanced Photon Source at Argonne National Laboratory. The acquired XANES data were processed according to standard procedures using the ATHENA software.

X-ray Photoelectron Spectroscopy: Photoelectron spectroscopy at the *O*-1s and Ni-2*p* core levels of NiO_x thin films was performed in Kratos AXIS ULTRA with a DLD detector at the Birck Nanotechnology Centre, Purdue University, USA. The sample was slightly heated around 50 °C during the time of measurement. The measurement was performed in an ultrahigh vacuum condition. The XPS measurements were conducted with Al Kα radiation (1486.6 eV). All XPS spectra were standardized with respect to carbon 1*s* peak (284 eV). The data were extracted and processed using CasaXPS software (http://www.casaxps.com/).

Midinfrared Near-Field Microscopy: Midinfrared s-SNOM was performed using a commercial setup (neaspec-GMBH) which was based on a tapping-mode atomic force microscopy with a cantilevered metal-coated tip of apex radius of ≈30 nm, oscillation frequency of $\Omega \approx 280$ kHz, and a tapping amplitude of ≈100 nm. A monochromatic quantum cascade laser beam at $\lambda = 10.5$ μm was focused at the tip by a parabolic mirror at angle of 45° to the sample surface. The detection method was based on phase modulation (pseudoheterodyne) interferometry and enabled detection of the backscattered light demodulated at higher harmonics of tip resonance frequency.[51,52]

Carrier Concentration Calculation from Midinfrared Near-Field Microscopy: To theoretically estimate the carrier concentration for each NiO_x sample in Figure 5c, we used the extended finite dipole model for layered systems[53–56] assuming a Drude-type dielectric function for NiO_x. The model describes the tip by a metallic ellipsoid which was illuminated at 45° relative to tip apex. The tip-scattered field was given by $E_s = se^{(i\varphi)} \propto (1 + r_p)^2 \alpha_{eff} E_{inc}$, where r_p is the far-field Fresnel reflection coefficient of the sample, E_{inc} the incident electric field, and α_{eff} the effective polarizability of the tip.[57,58] The free carrier densities n are included in r_p via the dielectric function of the NiO_x sample given by $\varepsilon_{NIO}(\omega) = \varepsilon_\infty - \frac{\omega_p^2}{\omega^2 + i\omega/\tau}$, where ε_∞ is the high-frequency dielectric function, $\omega_p = \sqrt{\frac{ne^2}{m^* \varepsilon_0}}$ is plasma frequency, $\tau = \frac{\sigma_0 m^*}{ne^2}$ is electron scattering time, m^* the effective mass, and σ_0 the conductivity.[59,60]

To estimate the carrier density (n), we fit the normalized experimental data point found by taking the ratio of signal value on NiO_x to signal value on Pd, ($s_2(NiO_x)/s_2(Pd)$) with the calculated normalized near-field amplitude ($s_2(NiO_x)/s_2(Pd)$), using the extended finite dipole model, and estimated the carrier densities n for each NiO_x sample in Figure 5c. This procedure gave $n = 1.96 \times 10^{18}\,cm^{-3}$ (as-prepared NiO_x), $n = 1.93 \times 10^{18}\,cm^{-3}$ (annealed at 350 °C), $n = 1.9 \times 10^{18}\,cm^{-3}$ (annealed at 400 °C), and $n = 1.87 \times 10^{18}\,cm^{-3}$ (annealed at 450 °C). This first-order estimate showed an expected trend, where the carrier concentration increases with increasing conductivity, NiO_x (annealed at 450 °C) has the smallest carrier density, and NiO_x (as prepared) shows the largest density.

First-Principles Electronic Structure Calculation of NiO_x for XANES Spectroscopy: Density functional theory (DFT) calculations[61,62] of NiO_x systems were performed using the Vienna ab initio Simulation Package (VASP)[63–65] with projector-augmented wave (PAW)[66] approach. The exchange-correlation functional used was the Perdew–Berke–Ernzerhof (PBE)[67]–generalize gradient approximation (GGA).[68,69] To model the strongly correlated Ni 3*d* states, Hubbard U[70] of 7.05 eV was used for Ni.[71] All calculations were performed using the Gaussian-smearing algorithm with the cutoff energy for the planewave basis set as 520 eV. Γ-centered k-point grids of 30 Å were used. All calculations were spin polarized, and their energy and atomic forces were converged to within 10^{-4} eV and 0.02 eV $Å^{-1}$, respectively. The O K-edge XANES spectra were computed using the FEFF9 package,[72] which implemented Green's formulation of the multiple scattering theory.

The initial NiO_x crystal structure with space group $Fm\bar{3}m$ (mp-19 009) was taken from Materials Project.[73] A $2 \times 2 \times 2$ supercell of NiO_x (32 atoms) was used to accommodate the symmetry of the antiferromagnetic ordering. Oxygen-deficient NiO_x was modeled by removing on O atom from the fully relaxed NiO_x supercell. The O K-edge XANES calculations were performed on all symmetrically distinct O sites in stoichiometric and oxygen-deficient NiO_x. For oxygen-deficient NiO_x, only O atoms less than 5 Å away from the oxygen vacancy defect were calculated as the XANES resembled that of stoichiometric NiO_x beyond 5 Å. The calculated site-wise XANES spectra were averaged to give the structure-wise spectra.

Simulation of Oxygen Migration during Training: The resistance of the NiO_x device was modulated by the concentration of oxygen at the interface at the top electrode. The resistivity of the channel was defined[74] as

$$\rho = \rho_0 e^{\frac{n-n_0}{n_d}} \tag{1}$$

where n is the concentration of mobile oxygen atom and ρ_0, n_0, and n_d are fitting parameters. The resistance of the device is defined as

$$R = \int_{x_1}^{x_2} \rho(x) - R_0 \tag{2}$$

where R_0 is an extra-fitting parameter that is used to simplify the fitting process, x_1 is the x-axis of the top electrode, and x_2 is the x-axis value at end of the interface region. The oxygen atoms' motion induced by the external potential was formulated by the drift-diffusion equation as follows.

$$\frac{\partial n}{\partial t} = \nabla.(D\nabla n - \nu n) + G \tag{3}$$

where D is the diffusion coefficient, and ν is the drift velocity that is defined as

$$\nu = \nu_0 e^{-\frac{E_a}{k_B T}} \sinh\left(\frac{qaE}{mk_B T}\right) \tag{4}$$

where E is the electric field, q is the electron charge, a is the hopping distance, m is fitting parameter, k_B is the Boltzmann's constant, T is the temperature, ν_0 is a fitting parameter, G is the generation term, and E_a is the diffusion barrier. The generation term G is added for sensitization defined as

$$G = A_G e^{-\frac{(E_a - q\beta E)}{k_B T}} \tag{5}$$

where A_G is the fitting parameter and β is the mesh size. The electric potential and the electric field were calculated by solving the current continuity equation.

$$\nabla.\frac{1}{\rho}\nabla\Psi = 0 \tag{6}$$

The differential Equation (1)–(6) is solved self-consistently[75] using the parameters' different values of the parameter (Figure S6, Supporting Information).

Simulation Methodology for Spiking Neural Network (SNN): The spiking neural network (SNN) was implemented using the PyTorch-based BindsNET,[49] an open-source library for designing biologically inspired algorithms. The network topology was the same as used in the study by Diehl et al.[48] with 225 neurons in the excitatory layer. The inputs were presented to the network as Poisson-encoded spikes, where the probability of spiking at any time step was proportional to the input pixel's value. A Poisson firing rate of 128 Hz was used. Each input image in the training set of 60 000 of the MNIST handwritten dataset[47] was presented for 100 ms. LIF neurons were used with the adaptive decay of the membrane potential modeled using the device characteristics. The decay rate was decreased by

Table 1. Simulation parameters for the SNN.

Parameter	Value
Post- and presynaptic learning rate, A_+, A_-	10^{-2}, 10^{-4}
Refractory period	5 ms
Time constant for STDP dynamics, τ	50.0
Weight range for the excitatory synapses	0.0–1.0
Synaptic weights from excitatory to inhibitory layer, $w_{exc-inh}$	22.5
Synaptic weights from inhibitory to excitatory layer, $w_{inh-exc}$	−240
Normalization factor	78.4

increasing the operating electric field of the device. Note that while this might impact the integration level of the neuron device, we considered that this could be offset by pulse width modulation of the input pulses to the neuron. Further device characterization studies had to be performed to validate this effect from a system formulation viewpoint. After each spike, the neuron was inhibited from firing again for a fixed refractory period, discarding any inputs that arrived meanwhile. The synaptic weights between the input and the excitatory layer are updated according to the standard spike-timing dependent plasticity (STDP) rule[76] of

$$\Delta w = \begin{cases} A_+ \exp\left(\frac{-\Delta t}{\tau}\right) \Delta t > 0 \\ -A_- \exp\left(\frac{\Delta t}{\tau}\right) \Delta t < 0 \end{cases} \quad (7)$$

where Δt is timing difference between pre- and postspikes, A_+ and A_- are the pre- and postsynaptic learning rates, and τ is the time constant of the STDP dynamics. The other connections between the layers ($w_{exc-inh}$, $w_{inh-exc}$) were kept fixed. The inhibitory layer was connected to the excitatory layer in a one-to-one manner and implemented the functionality of lateral inhibition. This ensured that different neurons learn different input patterns. Finally, we normalized the weights such that the neurons in the network were equally used.[77] We trained the network over the entire dataset for three epochs with a batch size of eight. Neurons were assigned classes based on their highest spiking rate. The network parameters used for training are listed in **Table 1**.

Supporting Information

Supporting Information is available from the Wiley Online Library or from the author.

Acknowledgements

This research used resources of the Advanced Photon Source, a U.S. Department of Energy (DOE) Office of Science User Facility operating for the DOE Office of Science by Argonne National Laboratory under contract no. DE-AC02-06CH11357 and additional support by National Science Foundation under grant no. DMR-0703406. S.M. thanks C. Huang, X. Chen, and T. J. Park for assistance in device fabrication and measurement. The authors acknowledge ARO grant W911NF1920237 and AFOSR FA9550-18-1-0250 for support. N.A., S.G., and Y.A. acknowledge support from the Air Force Office of Scientific Research (AFOSR), grant no. FA9559-16-1-0172 and National Science Foundation (NSF), grant no. 1904097. The X-ray absorption spectroscopy simulation study was supported by Quantum Materials for Energy Efficient Neuromorphic Computing (Q-MEEN-C), an Energy Frontier Research Center funded by DOE, Office of Science, BES under award no. DE-SC0019273. The authors also acknowledge computational resources provided by Triton Shared Computing Cluster (TSCC) at the University of California, San Diego, the National Energy Research Scientific Computing Centre (NERSC), and the Extreme Science and Engineering Discovery Environment (XSEDE) supported by National Science Foundation under grant no. ACI-1053575. A. N. M. N. I. and A. S.'s research was funded in part by the National Science Foundation (BCS #2031632 and CCF #1955815).

Conflict of Interest

The authors declare no conflict of interest.

Author Contributions

S.M., Z.Z., and S.R. conceived the project; S.M. and Z.Z. worked on NiO_x growth; S.M. fabricated the NiO_x thin-film devices and performed electrical habituation and sensitization measurements; S.G, N.A.A., and Y.A. conducted midinfrared nanoimaging; O.W. measured Raman spectroscopy; H.Z and F.R. performed X-ray absorption measurements; F.R. performed X-ray absorption near-edge structure measurement near the Ni L-edge and O K-edge of devices; S.M. and Z.Z. analyzed the X-ray absorption spectroscopy results; R.A. and K.R. conducted oxygen vacancy migration simulation; R.T, J.K., C.C., and S.P.O. perform the calculation of first-principles electronic structure of NiO_x absorption spectroscopy; A. N. M. N. I. and A. S. performed the spiking neural network simulations with unsupervised learning; and S.M., and S.R. wrote the manuscript. All authors discussed the results and commented on the manuscript.

Code Availability

The spiking neural network (SNN) learning simulation has been performed using PyTorch-based BindsNET and is available from the authors via proposal submission.

Data Availability Statement

The data that support the findings of this study are available on request from the corresponding author. The data are not publicly available due to privacy or ethical restrictions.

Keywords

neuromorphic devices

Received: March 10, 2022
Revised: June 29, 2022
Published online:

[1] T. M. Hennessey, W. B. Rucker, C. G. McDiarmid, *Anim. Learn. Behav.* **1979**, *7* 417.
[2] C. T. Fernando, A. M. Liekens, L. E. Bingle, C. Beck, T. Lenser, D. J. Stekel, J. E. Rowe, *J. R. Soc. Interface* **2009**, *6*, 463.
[3] R. P. Boisseau, D. Vogel, A. Dussutour, *Proc. R. Soc. B Biol. Sci.* **2016**, *283*, 2.
[4] C. Darwin, *On the Origin of Species by Means of Natural Selection, or the Preservation of Favoured Races in the Struggle for Life*, vol. *24*, 6th ed., B. (John Murray), London, no. 1st Edition, p. 502, http://promo.net/pg (accessed: November 1859).
[5] S. Ginsburg, E. Jablonka, *J. Biosci.* **2009**, *34*, 633.
[6] E. Jablonka, *Prog. Biophys. Mol. Biol.* **2013**, *111*, 99.
[7] G. M. Church, Y. Gao, S. Kosuri, *Science* **2012**, *337*, 1628.

[8] K. M. Berger, P. A. Schneck, *Front. Bioeng. Biotechnol.* **2019**, *7*, 17.
[9] N. D. Alien, M. L. Norris, M. A. Surani, *Cell* **1990**, *61*, 853.
[10] R. Holliday, *Dev. Genet.* **1994**, *15*, 453457.
[11] E. M. Ornitz, D. Guthrie, *Psychophysiology* **1989**, *26*, 166.
[12] B. G. Dias, S. A. Maddox, T. Klengel, K. J. Ressler, *Trends Neurosci.* **2015**, *38*, 96.
[13] E. M. Eisenstein, D. Eisenstein, J. C. Smith, *Integr. Physiol. Behav. Sci.* **2001**, *36*, 251.
[14] Z. Wang, S. Joshi, S. E. Savel'ev, H. Jiang, R. Midya, P. Lin, M. Hu, N. Ge, J. P. Strachan, Z. Li, Q. Wu, *Nat. Mater.* **2017**, *16*, 101.
[15] X. Yang, Y. Fang, Z. Yu, Z. Wang, T. Zhang, M. Yin, M. Lin, Y. Yang, Y. Cai, R. Huang, *Nanoscale* **2016**, *8*, 18897.
[16] Z. Wu, J. Lu, T. Shi, X. Zhao, X. Zhang, Y. Yang, F. Wu, Y. Li, Q. Liu, M. Liu, *Adv. Mater.* **2020**, *32*, 19.
[17] S. Marsland, *Neurobiol. Learn. Mem.* **2009**, *92*, 260.
[18] R. F. Thompson, *Neurobiol. Learn. Mem.* **2009**, *92*, 127.
[19] J. Schemmel, D. Brüderle, K. Meier, B. Ostendorf, in *Proc. - IEEE Int. Symp. Circuits Syst.*, IEEE, Piscataway, NJ **2007**, pp. 3367–3370.
[20] H. Zhao, W. Wang, X. Liu, B. Song, J. Diao, in *2018 IEEE 3rd Int. Conf. Signal Image Process. ICSIP 2018*, IEEE, Piscataway, NJ **2019**, pp. 24–27.
[21] F. Walter, F. Röhrbein, A. Knoll, *Neural Networks* **2015**, *72*, 152.
[22] P. A. Merolla, J. V. Arthur, R. Alvarez-Icaza, A. S. Cassidy, J. Sawada, F. Akopyan, B. L. Jackson, N. Imam, C. Guo, Y. Nakamura, B. Brezzo, *Science* **2014**, *345*, 668.
[23] Z. Zhang, S. Mondal, S. Mandal, J. M. Allred, N. A. Aghamiri, A. Fali, Z. Zhang, H. Zhou, H. Cao, F. Rodolakis, J. L. McChesney, *Proc. Natl. Acad. Sci.* **2021**, *118*, e2017239118.
[24] F. Zuo, P. Panda, M. Kotiuga, J. Li, M. Kang, C. Mazzoli, H. Zhou, A. Barbour, S. Wilkins, B. Narayanan, M. Cherukara, *Nat. Commun.* **2017**, *8*, 17.
[25] Y. Van De Burgt, E. Lubberman, E. J. Fuller, S. T. Keene, G. C. Faria, S. Agarwal, M. J. Marinella, A. Alec Talin, A. Salleo, *Nat. Mater.* **2017**, *16*, 414.
[26] C. S. Yang, D. S. Shang, N. Liu, E. J. Fuller, S. Agrawal, A. A. Talin, Y. Q. Li, B. G. Shen, Y. Sun, *Adv. Funct. Mater.* **2018**, *28*, 110.
[27] T. Ohno, T. Hasegawa, T. Tsuruoka, K. Terabe, J. K. Gimzewski, M. Aono, *Nat. Mater.* **2011**, *10*, 591.
[28] T. Chang, S. Jo, W. Lu, *ACS Nano* **2011**, *5*, 7669.
[29] S. G. Hu, Y. Liu, T. P. Chen, Z. Liu, Q. Yu, L. J. Deng, Y. Yin, S. Hosaka, *Appl. Phys. Lett.* **2013**, *103*, 1.
[30] E. N. Sokolov, *Annu. Rev. Physiol.* **1963**, *25*, 545.
[31] C. Pepino, C. Rakovski, C. Gutierrez, A. Rodriguez, S. Tillett, C. Berriman, M. Mason, A. W. Ingalls, R. Emshwiler, S. C. Scher, V. Zachary, *Neurobiol. Learn. Mem.* **2022**, *187*, 107542.
[32] H. Yildirim, R. Pachter, *ACS Appl. Mater. Interfaces* **2018**, *10*, 9802.
[33] R. C. Atkinson, R. M. Shiffrin, *Psychol. Learn. Motiv.* **1968**, *2*, 89.
[34] S. Seo, M. J. Lee, D. H. Seo, E. J. Jeoung, D. S. Suh, Y. S. Joung, I. K. Yoo, I. R. Hwang, S. H. Kim, I. S. Byun, J. S. Kim, *Appl. Phys. Lett.* **2004**, *85*, 5655.
[35] A. Liu, G. Liu, H. Zhu, B. Shin, E. Fortunato, R. Martins, F. Shan, *Appl. Phys. Lett.* **2016**, *108*, 233506.
[36] L. Y. Xie, D. Q. Xiao, J. X. Pei, J. Huo, X. Wu, W. J. Liu, S. J. Ding, *Mater. Res. Express* **2020**, *7*, 046401.
[37] E. Arciga-Duran, Y. Meas, J. J. Pérez-Bueno, J. C. Ballesteros, G. Trejo, *Electrochim. Acta* **2018**, *268*, 49.
[38] B. Zhao, X. K. Ke, J. H. Bao, C. L. Wang, L. Dong, Y. W. Chen, H. L. Chen, *J. Phys. Chem. C* **2009**, *113*, 14440.
[39] S. Oswald, W. Brückner, *Surf. Interface Anal.* **2004**, *36*, 17.
[40] Y. Zhou, X. Guan, H. Zhou, K. Ramadoss, S. Adam, H. Liu, S. Lee, J. Shi, M. Tsuchiya, D. D. Fong, S. Ramanathan, *Nature* **2016**, *534*, 231.
[41] R. Berdan, E. Vasilaki, A. Khiat, G. Indiveri, A. Serb, T. Prodromakis, *Sci. Rep.* **2016**, *6*, 19.
[42] A. Cyr, M. Boukadoum, *Bioinspiration Biomimetics* **2013**, *8*, 016007.
[43] W. Zhang, D. J. Linden, *Nat. Rev. Neurosci.* **2003**, *4*, 885.
[44] S. Ghosh-dastidar, A. G. Lichtenstein, *Int. J.* **2009**, *19*, 295.
[45] B. Rajendran, Y. Liu, J. S. Seo, K. Gopalakrishnan, L. Chang, D. J. Friedman, M. B. Ritter, *IEEE Trans. Electron Devices* **2013**, *60*, 246.
[46] G. Indiveri, in *Proc. 2003 Int. Symp. Circuits and Systems, 2003. ISCAS '03*, Vol. *4*, Bangkok, Thailand **2003**, pp. IV-820–IV-823, https://doi.org/10.1109/ISCAS.2003.1206342.
[47] Y. LeCun, C. Cortes, C. J. C. Burges, *The MNIST Database of Handwritten Digits*, Modified National Institute of Standards and Technology (MNIST), New York, USA **1998**, *10*, 14, http//yann.lecun.-com/exdb/mnist.
[48] P. U. Diehl, M. Cook, *Front. Comput. Neurosci.* **2015**, *9*, 99.
[49] H. Hazan, D. J. Saunders, H. Khan, D. Patel, D. T. Sanghavi, H. T. Siegelmann, R. Kozma, *Front. Neuroinf.* **2018**, *12*, 118.
[50] S. Dutta, A. Saha, P. Panda, W. Chakraborty, J. Gomez, A. Khanna, S. Gupta, K. Roy, S. Datta, *Dig. Tech. Pap. - Symp. VLSI Technol.* **2019**, *2019*, T140.
[51] Y. Abate, D. Seidlitz, A. Fali, S. Gamage, V. Babicheva, V. S. Yakovlev, M. I. Stockman, R. Collazo, D. Alden, N. Dietz, *ACS Appl. Mater. Interfaces* **2016**, *8*, 23160.
[52] A. Fali, S. Gamage, M. Howard, T. G. Folland, N. A. Mahadik, T. Tiwald, K. Bolotin, J. D. Caldwell, Y. Abate, *ACS Photonics* **2021**, *8*, 175.
[53] A. Cvitkovic, N. Ocelic, R. Hillenbrand, *Opt. Express* **2007**, *15*, 8550.
[54] N. A. Aghamiri, F. Huth, A. J. Huber, A. Fali, R. Hillenbrand, Y. Abate, *Opt. Express* **2019**, *27*, 24231.
[55] A. Fali, S. T. White, T. G. Folland, M. He, N. A. Aghamiri, S. Liu, J. H. Edgar, J. D. Caldwell, R. F. Haglund, Y. Abate, *Nano Lett.* **2019**, *19*, 7725.
[56] B. Hauer, A. P. Engelhardt, T. Taubner, *Opt. Express* **2012**, *20*, 13173.
[57] L. M. Zhang, G. O. Andreev, Z. Fei, A. S. McLeod, G. Dominguez, M. Thiemens, *Phys. Rev. B: Condens. Matter Mater. Phys.* **2012**, *85*, 18.
[58] A. A. Govyadinov, I. Amenabar, F. Huth, P. Scott Carney, R. Hillenbrand, *J. Phys. Chem. Lett.* **2013**, *4*, 1526.
[59] M. D. Irwin, J. D. Servaites, D. B. Buchholz, B. J. Leever, J. Liu, J. D. Emery, M. Zhang, J. H. Song, M. F. Durstock, A. J. Freeman, M. J. Bedzyk, *Chem. Mater.* **2011**, *23*, 2218.
[60] K. V. Rao, A. Smakula, *J. Appl. Phys.* **1965**, *36*, 2031.
[61] P. Hohenberg, W. Kohn, *Phys. Rev.* **1964**, *136*, B864.
[62] W. Kohn, L. J. Sham, *Phys. Rev. B* **1965**, *140*, A1133.
[63] G. Kresse, J. Hafner, *Phys. Rev. B* **1993**, *47*, 558.
[64] G. Kresse, J. Furthmüller, *Comput. Mater. Sci.* **1996**, *6*, 15.
[65] G. Kresse, J. Furthmüller, *Phys. Rev. B* **1996**, *54*, 11169.
[66] P. E. Blöchl, *Phys. Rev. B* **1994**, *50*, 17953.
[67] J. P. Perdew, K. Burke, M. Ernzerhof, *Phys. Rev. Lett.* **1996**, *77*, 3865.
[68] D. C. Langreth, M. J. Mehl, *Phys. Rev. B* **1983**, *28*, 1809.
[69] A. D. Becke, *Phys. Rev. A* **1988**, *38*, 3098.
[70] V. I. Anisimov, J. Zaanen, O. K. Andersen, *Phys. Rev. B* **1991**, *44*, 943.
[71] S. Mandal, K. Haule, K. M. Rabe, D. Vanderbilt, *npj Comput. Mater.* **2019**, *5*, 1.
[72] J. J. Rehr, J. J. Kas, F. D. Vila, M. P. Prange, K. Jorissen, *Phys. Chem. Chem. Phys.* **2010**, *12*, 5503.
[73] A. Jain, S. P. Ong, G. Hautier, W. Chen, W. D. Richards, S. Dacek, S. Cholia, D. Gunter, D. Skinner, G. Ceder, K. A. Persson, *APL Mater.* **2013**, *1*, 011002.
[74] D. Kawamoto, A. N. Hattori, M. Yamamoto, X. L. Tan, K. Hattori, H. Daimon, H. Tanaka, *ACS Appl. Electron. Mater.* **2019**, *1*, 82.
[75] S. Kim, S. J. Kim, K. M. Kim, S. R. Lee, M. Chang, E. Cho, Y. B. Kim, C. J. Kim, U. In Chung, I. K. Yoo, *Sci. Rep.* **2013**, *3*, 16.
[76] G. Q. Bi, M. M. Poo, *J. Neurosci.* **1998**, *18*, 10464.
[77] G. J. Goodhill, H. G. Barrow, *Neural Comput.* **1994**, *6*, 255.